Surveillance nanotechnology for multi-organ cancer metastases

Harini Kantamneni[5,#], **Margot Zevon**[1,#], **Michael J. Donzanti**[1], **Xinyu Zhao**[2], **Yang Sheng**[2], **Shravani R. Barkund**[1], **Lucas H. McCabe**[6], **Whitney Banach-Petrosky**[3], **Laura M. Higgins**[1], **Shridar Ganesan**[3], **Richard E. Riman**[4], **Charles M. Roth**[1,5], **Mei-Chee Tan**[2], **Mark C. Pierce**[1,*], **Vidya Ganapathy**[1,*], and **Prabhas V. Moghe**[1,5,*,#]

[1]Department of Biomedical Engineering, Rutgers University, 599 Taylor Road, Piscataway, NJ 08854

[2]Engineering Product Development, Singapore University of Technology and Design, 8 Somapah Rd, Singapore 487372, Singapore

[3]Rutgers Cancer Institute of New Jersey, 195 Little Albany Street, New Brunswick, NJ 08903

[4]Department of Materials Science and Engineering, Rutgers University, 607 Taylor Road, Piscataway, NJ 08855

[5]Department of Chemical & Biochemical Engineering, Rutgers University, Piscataway, NJ 08854, USA

[6]Department of Computer Science, Rutgers University, Piscataway, NJ 08854, USA

Abstract

The identification and molecular profiling of early metastases remains a major challenge in cancer diagnostics and therapy. Most in vivo imaging methods fail to detect small cancerous lesions, a problem that is compounded by the distinct physical and biological barriers associated with different metastatic niches. Here, we show that intravenously injected rare-earth-doped albumin-encapsulated nanoparticles emitting short-wave infrared light (SWIR) can detect targeted metastatic lesions in vivo, allowing for the longitudinal tracking of multi-organ metastases. In a murine model of basal human breast cancer, the nanoprobes enabled whole-body SWIR detection of adrenal gland microlesions and bone lesions that were undetectable via contrast-enhanced magnetic resonance imaging (CE-MRI) as early as, respectively, three weeks and five weeks post-inoculation. Whole-body SWIR imaging of nanoprobes functionalized to differentially target

Corresponding Authors: Prabhas V. Moghe, PhD., Vidya Ganapathy, PhD., & Mark C. Pierce, PhD.
#H. Kantamneni and M. Zevon are equal first co-authors
#*Contact Author:* Prabhas Moghe, PhD, Distinguished Professor of Biomedical Engineering, moghe@rutgers.edu; Phone: 908-230-0147

Competing interests

The authors declare no competing financial interests.

distinct metastatic sites and administered to a biomimetic murine model of human breast cancer resolved multi-organ metastases that showed varied molecular profiles at the lungs, adrenal glands and bones. Real-time surveillance of lesions in multiple organs should facilitate pre-therapy and post-therapy monitoring in preclinical settings.

Keywords

cancer metastasis; nanotechnology; shortwave infrared imaging; rare earths

---

Metastasis is the primary cause of breast cancer deaths,[1,2] where the median survival rate for patients with multi-organ metastases is less than two years[1]. Currently about 10% of clinical cases present distal metastatic disease at diagnosis, and 20–40% develop distal metastasis within five years[3,4]. The bones remain the most common site of distant metastasis in breast cancer, accounting for about 70% of diagnosed cases[5,6] followed by the liver, lungs, adrenal glands, and brain. To improve patient prognosis and survival rate, robust surveillance techniques and lesion site-specific therapies are needed. In this work, we report an integrated cancer-surveillance system based on the design of nanoscale photonic probes for differential accumulation at distinct metastatic sites, coupled with deep-tissue optical detection of emergent lesions (Figure 1). We demonstrate the efficacy of this approach by longitudinal surveillance of multi-organ metastatic signatures in biomimetic metastatic murine models[7,8].

The detection of early, multi-organ cancer metastasis is a significant challenge because distinct sites rely on unique mechanisms of microcirculation. The functional design of nanoscale probes to detect metastases needs to account for differences in the infiltration barriers and microenvironment of individual target sites. For instance, passive nanoparticle targeting to a distant site such as the bone marrow exploits the discontinuous fenestrated sinusoid capillaries and an almost absent basement membrane to increase nanoparticle infiltration[9]. In contrast, other distal sites such as the adrenal glands are not permissive to passive nanoparticle infiltration due to their continuously fenestrated sinusoid capillaries and a tight basement membrane. In this case, active functionalization of nanoparticles is necessary to achieve targeted delivery to the metastatic niche[10]. In this study, we tailored the physiochemical properties of nanoparticle formulations based on published[11,12] tumor and distal organ pathophysiology for site-specific accumulation and simultaneous detection of multi-organ metastasis, specifically to the bone, lungs and the adrenal glands[11,12].

New classes of optical imaging agents that exhibit improved tissue transmittance and deep tissue penetration[13,14] are candidates for imaging micro-metastases. We designed imaging probes based on rare-earth albumin nanocomposites (ReANCs), which are ceramic rare-earth (Re) doped particles encapsulated in human serum albumin. These probes emit short wave infrared (SWIR) light[15], which has several advantageous properties for biological imaging[16,17]. The lack of excitation-emission band overlap and elimination of tissue autofluorescence produces significantly improved signal-to-noise ratios[15], while the narrow emission bands of the rare-earths allows for multiplexed labeling. In this study, we exploit the optical emissions of ReANC probes in the SWIR (or (Near InfraRed) NIR II) window[18]

(900 – 1,700 nm), which is characterized by deep penetration through tissue[19] and reduced loss of spatial resolution due to scattering.

We initially sought to resolve micro-metastatic bone lesions *in vivo* in a biomimetic model of basal breast cancer by intravenous administration of ReANC probes. The goal was to demonstrate that SWIR-based surveillance is more robust for emergent metastases than conventional imaging modalities such as MRI or Computed Tomography (CT). Next, we challenged our surveillance technology using a biomimetic model of metastatic breast cancer, which results in metastases at different anatomical sites and also shows dichotomous molecular profiles at these sites[18]. Figure 1 illustrates a non-invasive surveillance system that provides an integrated imaging system to track multi-organ metastases for xenogeneic and potential patient-derived models of cancer. This approach integrates distinct SWIR-emitting nanoparticles each designed to penetrate different metastatic organs and to enable longitudinal tracking of lesion development. The use of this surveillance system in the clinic will lead to major advances in altering and tailoring patient-specific niche-based therapeutic regimen.

RESULTS

Design and Characterization of C-X-C Chemokine Receptor type 4 (CXCR4)-Targeted Photonic Nanoparticles

The dopant-host chemistries and heterostructure of rare-earth-doped nanoparticles govern their optical emission wavelengths and efficiencies,[16,20] which have been optimized in our previous work[15,17]. Rare-earth nanoparticles synthesized via a burst nucleation reaction,[20,21] were incorporated into rare-earth albumin nanocomposites (ReANCs) via solvent-induced controlled coacervation of albumin[22] (Supplementary Figure 1a). The sizes of the rare-earth nanoparticles (~18–25 nm diameter) and ReANCs (85–100 nm diameter) were tailored by controlling the reaction chemistry and kinetics to allow for the size-dependent Enhanced Permeation and0 Retention effect(EPR) (at approximately below 100 nm) to permit passive targeting[11]. ReANCs were also engineered to actively target tissues such as the adrenal glands where the microcirculation prevents passive uptake. Briefly, functionalized ReANCs (fReANCs) were generated by decorating the surface of ReANCs with AMD3100, a small molecule antagonist of the chemokine receptor and cancer biomarker CXCR4[23,24]. AMD3100 was adsorbed onto the surface of ReANCs to use native drug binding pockets on human serum albumin[25,26]. Dynamic light scattering (DLS) analysis revealed monodisperse populations and minimal change in hydrodynamic diameter of fReANCs compared to ReANCs (Supplementary Figure 1b). Nanoparticle yield was quantified as approximately 58% using the Bicinchoninic acid Assay(BCA) protein assay. AMD3100 loading efficiency was determined to be 70% by High-Performance Liquid Chromatography (HPLC), consistent with our previous study[19]. The functionalized ReANCs demonstrated active targeting as validated by competitive CXCR4 blockage and inhibition of cancer cellular migration assays (Supplementary Figures 2 and 3). Both native and functionalized ReANC formulations have exhibited no overt toxicity[15,19], which is consistent with our findings of no or little change in body weight (data not shown). Histopathology of major organs of clearance like liver, lung, kidney and spleen extracted at various time points post

nanoparticle injection shows no abnormalities in tissue architecture (Supplementary Figure 4). Additionally, normal histopathology from the organs of accumulation such as the liver and lungs following repeated weekly administration of nanoparticles (Supplementary Figure 5) indicates no signs of nanoparticle toxicity. Liver, lungs and the spleen seem to be major organs of accumulation based on yttrium content per gram of tissue correlated to the content in injected dose as determined by Inductively Coupled Plasma-Mass Spectrometry (ICP/MS) (Supplementary figure 6a). The clearance pattern of ReANCs from animals, determined using ICP/MS, shows a decrease in nanoparticle content from all organs over the course of 7 days. Accumulation in the spleen increased until day 3, after which the nanoparticle content began to decline, indicating clearance (Supplementary Figure 6b). The ICP/MS data shows correlation to the ex vivo SWIR signal from these respective organs (Supplementary Figure 6c and d).

SWIR imaging of photonic nanoparticles discerns bone lesions *in vivo* that are undetectable by MRI and CT

Detection of micro-metastatic lesions in the bone marrow is challenging due to a lack of sensitive imaging modalities[27]. Current approaches can successfully detect abnormal bone activity, but are unable to identify cancer-related activity associated with bone metastases. Thus, there is a need for targeted imaging agents that enable sensitive imaging of the earliest metastatic cell clusters at otherwise inaccessible metastatic niches.

Female athymic nude mice were injected with bone-tropic MDA-MB-231 derived SCP2 cells in the intratibial cavity (Figure 2a). Animals received weekly injections of unfunctionalized ReANC probes, beginning a week after tumor cell inoculation and were monitored using a pre-clinical SWIR imaging system (Figure 2b and c)[15]. Longitudinal imaging showed greater than 2–fold higher SWIR fluorescence in tumor-bearing animals compared to healthy controls, from 5 weeks' post-inoculation until the study endpoint (Figure 2d). SWIR-imaging-based detection of tumors in the tibial cavity was validated by whole body Bio-Luminescence Imaging (BLI) (Figure 2e). *Ex vivo* SWIR imaging of the skeletons at end point confirmed accumulation of ReANC probes in the bone space (Supplementary Figure 7). Notably, tumor lesions were barely discernible using common preclinical imaging modalities such as CT and MRI (Figures 2f and g), even at the study end point. Additionally, *ex vivo* Hematoxylin & Eosin (H&E) staining of tumor-bearing bone showed hypocellularization when compared to healthy controls, indicative of tumor-cell mediated lytic activity in the bone (Figure 2h).

Distal bone lesions can be detected with SWIR imaging earlier than MRI in a biomimetic basal-like breast cancer metastasis model

Having successfully imaged small clusters of tumor cells in a *localized intratibial model*, we examined the ability of whole body SWIR imaging to discern metastatic lesions in a breast cancer bone metastasis model. We established a MDA-MB-231 model previously shown by Minn *et al.* to follow different seeding kinetics and to colonize the lungs and bones following intravenous administration[18,28]. This model exhibits low metastatic burden in the bones and hind legs in contrast with a relatively high burden in the lungs[28,29]. We inoculated female athymic nude mice with MDA-MB-231 derived SCP28 cells via tail vein, followed by

weekly injection of ReANCs for SWIR imaging (Figure 3a and supplementary video 1). Compared to healthy controls (Figure 3b), tumor-bearing animals (Figure 3c) revealed a greater than two-fold increase in SWIR signal from the long bones, beginning at week-5 post-inoculation (Figure 3d). Most significantly, by week-9 we observed a greater than 5-fold increase in SWIR signal from the bones of tumor-bearing animals compared to controls (Figure 3d), while MRI still showed no abnormalities in the bone space (Figures 3e) and BLI showed absence of tumor burden in the bone (Figure 3f).

Nanoparticles encounter the lungs as their first barrier organ when administered intravenously, making the architecture of the lung vasculature an important determinant in their subsequent biodistribution to distant sites. A possible hypothesis for increased accumulation of ReANCs in the bone in this biomimetic model (Figure 3) compared to the previous intratibial model (Figure 2) could be that an altered vascular architecture due to tumor lesions in the lung is responsible for differences in nanoparticle biodistribution[30]. MRI analysis also revealed moderate tumor burden in the lungs (31.3 ± 25.4 mm^3). Previous studies have shown passive uptake of ReANCs in the lungs only when the lesions were large and highly vascularized[19]. During the studies reported here, no discernible SWIR signal from the lungs was detected (Figures 3c and d). This lack of lung signal reinforces the need to engineer nanoparticles for targeted uptake to organs such as lungs and adrenal glands where the infiltration barrier prevents passive uptake[12].

Differential niche-based accumulation of ReANC and fReANC formulations leads to multi-organ detection of metastases in a luminal breast cancer model

While bone physiology favors the uptake of nanoparticles such as ReANCs (Figures 2 and 3), other tissues require active targeting to facilitate nanoparticle labeling. In addition, cancer patients with metastases at multiple sites frequently have a lower quality of life and poorer prognosis than those with a single distant lesion[31]. Therefore, it is imperative that metastasis imaging agents be designed to label phenotypically distinct lesions at physiologically distinct sites. To this end, we hypothesized that fReANC's targeting the CXCR4 biomarker and non-targeted ReANC's could provide differential labeling of lesions at distinct organ sites in a biomimetic model of breast cancer metastasis.

The MCF-7 derived human metastatic breast cancer line was shown to express CXCR4 (Supplementary Figure 8). Athymic nude mice received intracardiac injections of MCF-7 cells to the left ventricle (Figure 4a). This model of luminal breast cancer is known to phenocopy human disease, leading to both adrenal and bone metastases in mice supplemented with estrogen[7]. Animals were given weekly injections of either fReANC's targeted to CXCR4 or non-targeted ReANCs, followed by SWIR imaging in both supine and dorsal positions. fReANCs preferentially accumulated in adrenal tumors (Figures 4b and d), exemplified by an almost 15-fold increase in SWIR intensity at this site in tumor-bearing animals compared to healthy controls, even as early as 3-weeks post-inoculation (Figure 4b–d). Notably, there was no significant difference between SWIR signal intensity in tumor-bearing versus healthy control animals when unfunctionalized ReANC's were used (Figure 4b, c and e). In contrast, we observed a 4-fold increase in SWIR signal from the bones of tumor-bearing animals as compared to healthy controls (Figures 5a and b) when

unfunctionalized ReANC's were administered for imaging. In this case, SWIR signal from the bones of animals receiving fReANC's was not elevated compared to healthy controls (Figure 5b).

The progression and location of metastases was monitored with bi-monthly MRI and validated by *in situ* and *ex vivo* SWIR imaging (Supplementary Figures 9 and 10). The smallest adrenal tumors detected by SWIR imaging were 7.8 mm^3 in volume following fReANC administration and 15.7 mm^3 with ReANC's, confirming the ability of fReANC's to target and resolve smaller metastatic clusters when compared to untargeted ReANC's. Fixed tissue sections were stained for estrogen receptor and confirmed the presence of tumors in the adrenal glands (Supplementary Figures 11 and 12).

While we were able to demonstrate differential accumulation of the nanoprobes in distinct metastatic organ sites, another goal of this nanotechnology system is to enable surveillance of multi-organ metastases within the same animal. To this end, we injected a cocktail of untargeted and targeted nanoprobes in a triple negative metastatic breast cancer mouse model. The MDA-MB-231 metastatic xenograft model leads to lung and bone metastases when cells were inoculated intravenously into the animal followed by injection of a cocktail of ReANCs and fReANCs (Figure 6a). We were able to reproduce enhanced localization of targeted nanoprobes to lungs (Figure 6b) and untargeted probes to leg lesions (Figure 6c) as evidenced by statistically significant higher SWRI signal in tumor-bearing compared to healthy controls. In a pilot study, we observed qualitative evidence of preferential accumulation of ReANCs (Figure 6d) in the leg and fReANCs in the lungs (Figure 6e). Notably, we demonstrate accumulation in both lungs and legs when a cocktail of ReANCs and fReANCs were co-administered (Figure 6f and g). Future studies will work on dose optimization and mechanistic insights for active and passive targeting of the nanoprobes in the same animal.

Superior resolution with SWIR imaging compared to CE-MRI for bone lesion detection in a biomimetic mouse metastatic model

SWIR imaging using ReANCs could detect bone lesions in orthotopic and metastatic models of breast cancer. We demonstrated that these bone lesions were undetectable by conventional MRI. However, in order to make a direct quantitative comparison to assess superior resolution with SWIR emitting nanoprobes, we performed CE-MRI studies in an experimental metastatic triple negative breast cancer model with metastases to both lungs and bone. We proposed to use detection of lung lesions prior to and post-contrast as positive control for CE-MRI. We injected ReANCs bi-weekly to monitor SWIR signal in bones of animals. Bi-weekly MRI using contrast was performed in parallel for comparison.

In particular, we are able to detect bone lesions at week 6 post-inoculation of tumor cells as evidenced by a statistically significant, two-fold increase in SWIR emission in comparison to non-tumor control animals. We also demonstrate that these lesions were not detectable by contrast-enhanced MRI at week 6 (Figure 7a and b) and that the apparent increase in MRI signal is not statistically significant until week 8 (Figure 7d). Most notably, SWIR emission in tumor-bearing animals was visualized two weeks before and with far greater fold increase in signal than CE-MRI (Figure 7c). Quantitative changes with contrast-enhanced MRI

between non-tumor controls and tumor-bearing animals were statistically not significant at week 6. Additionally, as a control for contrast-enhancement, we quantified MRI-contrast intensity in kidneys and found no significant change between tumor-bearing and non-tumor controls (Supplementary figure 13). Contrast-enhancement of lung lesions was used as positive control (Figure 7e and f).

Distinct metastatic lesions originating from a common cell line exhibit niche-dependent molecular signatures

Because the metastatic microenvironment of each pre-metastatic niche can cause site-specific variations in protein signatures, the ability for imaging agents to parse such site-specific molecular profiles will have far-reaching pre-clinical and clinical impact in developing diagnostic tools and therapeutic interventions in recurrent cancers. To further elucidate the role of the metastatic niche on the phenotypic signatures of metastatic lesions, cells were harvested from bones (MCF7-5624a and SCP28), adrenal glands (MCF7-6124A) and lungs (SCP28) in the metastatic tumor models (Supplementary Figure 14a). Cell lysates extracted from these were analyzed for differences in protein expression. In the luminal breast cancer model, analysis of microarray pixel density revealed upregulation of N-Cadherin, ADAM17, and JAM-A in adrenal-tropic cells (Supplementary Figure 14b), while bone-tropic cells were found to upregulate a separate set of markers, including Notch-1, amphiregulin, and EGF-R (Table 1).

Bone-tropic 5624a cells expressed a 2-fold increase in Notch-1 relative to adrenal-tropic cells. Notch-1 upregulation has previously been correlated with bone metastases and the presence of lytic lesions[32], while N-cadherin is associated with tumor invasiveness, growth, and metastasis[33]. Adrenal-tropic cells exhibited a 4.75-fold increase in N-cadherin expression compared with bone-tropic cells, suggestive of a more aggressive tumor phenotype.

In the triple negative breast cancer model (SCP28), we found niche-based differences in protein expression in the lung-tropic and bone-tropic lines using a human oncology array. We found in the lung-tropic line upregulation of metastasis-associated proteins such as Amphiregulin, Endoglin, and Carbonic Anhydrase-IX (Supplementary Figure 14c). Interestingly, the bone-tropic cells showed upregulation of two of the proteins present in the lung niche-signature namely Amphiregulin and Endoglin. Additionally, we found an increase in MMP3 and EpCAM in the bone-niche (Supplementary Figure 14d). The significant differences observed in molecular signatures between cell populations at various metastatic sites correlate with our ability to target these two metastatic lesions using divergent design criteria for our SWIR-emitting nanoparticles. These distinct molecular signatures also exemplify potential targets to develop niche-specific targeted nanoparticles for imaging and therapy.

DISCUSSION

Cancer metastasis is a process whose dynamics remain poorly understood due to the limited ability of existing techniques to obtain meaningful information in real-time. Optical imaging of metastasis in live animals under native physiological conditions has been innately difficult

due to poor tissue penetration and high background levels due to tissue autofluorescence. Most pre-clinical imaging in multi-organ metastatic models has been invasive, using intravital imaging windows and genetically engineered cells that express luciferase or fluorescent reporters[34–37]. The goal of this work was to develop an optical imaging system that could resolve multi-organ lesions at distant metastatic sites in real-time without necessitating genetically altered reporter cells.

We demonstrated that appropriately sized rare earth albumin nanocomposites are able to home to micro-metastatic lesions in the long bones (Figures 2, 3, and 5) and spine (Represented in supplemental video 1) in multiple *in vivo* breast cancer models. Because of robust nanocomposite accumulation and deep-tissue imaging SWIR emissions, micro-metastatic lesions were observed as early as three-weeks post-inoculation in an orthotopic model of breast cancer. We demonstrated that weekly injection of ReANC's showed consistent, rapid accumulation in the bones with complete clearance by 48h post-injection (Supplementary Figure 7), rendering the nanoprobes safe for repeated use in longitudinal studies. Notably, the ReANC probes elicited no overt toxicity when compared to controls (Supplementary Figures 4 and 5) and control animals showed no signs of distress during the study period. The clearance of ReANCs through major organs of clearance was within acceptable limits upto 7 days post-administration of probes (Supplementary Figure 6). Remarkably, MRI and CT did not reveal any changes in bone architecture. Histopathology also validated regions of possible changes in bone architecture when compared to tissue sections from control animals. Most notably, CE-MRI did not show significant quantitative changes at week 6, when bone lesions detected by SWIR imaging were significant between tumor-bearing versus control animals (Figure 7).

In a biomimetic model where multi-organ metastases to the lung and bone are observed, we found differential accumulation of ReANCs to lesions in the bone as early as 3-weeks post-inoculation. This was consistent with our previous findings, where ReANCs could not discern lung metastases until lesion volume reached around 56 mm^3 [19]. Bone lesions were undetectable on MRI and BLI whereas lung lesions were detected by MRI and BLI. Differential uptake of nanoparticles based on size[15,38] and surface functionalization[38] has been demonstrated in previous *in vitro* and *in vivo* studies. An added benefit of the differential nanoparticle uptake, especially via active targeting, is that we can quickly reduce the percentage of particles remaining in systemic circulation therefore achieving further reduction in unwanted background signal. Of particular interest in metastasis imaging would be a nanoparticle formulation that can be modified and administered systemically to detect distal multi-organ metastases in real-time. Simultaneous detection of metastases at multiple distinct sites is important for effective treatment as undetected lesions lead to recurrent disease. These persistent tumors are often resistant to therapy and require lesion-specific intervention[39]. The ability to detect phenotypically distinct tumors at distant sites is critical in predicting the likelihood of recurrence and in selection of effective therapies[28,29].

Intrinsic to the nanoprobe detection of multi-organ metastases is the design of multivariate targeting mechanisms. In order for the ReANC nanoprobes to penetrate through barriers in organs such as lungs, the design strategy would call for the display of a surface charge (to undergo transcytosis) or a targeting ligand (especially for charge-neutral particles such as

human serum albumin coated probes) to exhibit receptor mediated-endocytosis[40]. Other reports highlight the role of size, charge, shape and targeting ligand selection in altering nanoparticle infiltration through various barriers leading to the tumor in an animal model[41,42]. In our study, a combination of passive and active targeting may be key to the detection of tumors in the bones and adrenal glands, respectively. Sinusoid capillary fenestrations play a major role in nanoparticle delivery and, in combination with leaky vasculature of tumors, this could play a role in the increased accumulation of unfunctionalized ReANCs in the bone. Additionally, the changes in bone architecture associated with tumor progression may also play a role in improved accumulation of ReANCs to the bone. In contrast, the adrenal glands showed poor accumulation of unfunctionalized ReANCs along with pronounced recruitment of the functionalized fReANCs, which indicates the role of active targeting. The active targeting of our functionalized fReANCs is designed based on elevated CXCR4 binding (validation in Supplementary Figures 2 and 3). Tumor-targeted fReANCs were able to resolve adrenal lesions as small as 8 mm^3 and detect these lesions earlier than ReANCs, suggesting that the continuous fenestration of capillaries around adrenal tissue is not amenable for EPR of ReANCs. This result, combined with our previous studies in a lung metastasis model, indicates that ReANCs require a certain tumor burden in certain niches for accumulation, whereas sites such as the bone permit uptake with a relatively low tumor burden. To explore the relevance of our probes to a different metastatic model, we tested accumulation of fReANCs upon intravenous inoculation of MDA- MB-231 cells. Here, we demonstrated using a pilot study, that the probes can effectively resolve a different profile of multi-organ metastases (actively targeted fReANCs bound to metastases in the lungs versus passively targeted ReANCs accumulated in the bone) (Figure 6). Future studies could exploit these differences to explore the use of our imaging tools to further track nanoparticle penetration through the vascular, perivascular and interstitial space in tumors.

Understanding the molecular basis of interactions between a primary tumor, distant metastases, and the metastatic niche is critical to fulfill the promise of improved and personalized therapies in cancer patients. Our study highlights an integrated approach to enable sensitive and accurate detection and analysis of micro-metastatic lesions. Proteomic analysis of cells isolated from metastatic sites highlighted by distinct classes of our nanoprobes showed a clear dichotomy in molecular signatures. Specifically, increased Notch1 in bone lesions vis-à-vis N-cadherin in adrenal gland metastases provides molecular context to the metastatic process that can potentially be exploited for tailoring precision therapeutics to individual patients. Notably, early detection of lesions facilitated extraction and analysis of changes in niche-based signatures from tumor-onset to endpoint. Collectively, these outcomes provide us with a diagnostic tool with which we can longitudinally perform non-invasive molecular assessment of metastases and also monitor treatment outcomes targeted to highly heterogeneous metastatic lesions[29,43].

In summary, we have developed an integrated multi-organ metastasis imaging system for detection and analysis of early metastatic lesions in distal organs. We demonstrated the applicability of this imaging system in several distinct *in vivo* breast cancer models. Future pre-clinical applications of this approach will expand on the customization of ReANC probes with markers specific for metastatic lesions, based on the niche surrounding these

clusters. Researchers could design a cocktail of such site-interactive ReANC formulations to detect, track, and understand interactions between cells in these different compartments, providing clues that will eventually lead to development of better therapeutic agents for the clinic. As a whole-body surveillance system, we envision this to be a scanning imaging tool for pre- and post- therapy monitoring in preclinical settings, by real-time non-invasive molecular detection of lesions in multiple organs.

METHODS

Fabrication of rare-earth nanoparticles

Rare-earth nanoparticles were synthesized as previously described via burst nucleation reaction[15,20,21], and incorporated into rare-earth albumin nanocomposites (ReANCs) via solvent-induced controlled coacervation of albumin[15,22]. Hydrodynamic diameters of ReANCs were determined via dynamic light scattering (DLS) (Malvern Instruments Inc, UK) (Supplementary Figure 1A), which also revealed monodisperse particle populations. Two classes of ReANCs were designed for targeting distinct classes of metastatic sites. Albumin-based ReANCs were administered as unfunctionalized composites for detection of bone cancer metastases. In contrast, functionalized probes (fReANCs) were designed for targeting of adrenal gland metastases. fREANCs were generated through passive absorption of the CXCR4-antagonist AMD3100 (EMD Millipore, Darmstadt, Germany) onto the surface of fully formed ReANCs. A range of AMD3100 concentrations from 12.5 μM to 12.5 nM were generated for *in vitro* testing to determine the optimal loading conditions[19]. An AMD3100 loading concentration of 1.25 μM was used for all *in vivo* experiments. Nanoprobe diameter and polydispersity were determined through DLS; nanoprobe yield was determined by BCA protein assay.

In vivo imaging

Imaging studies were conducted using athymic nude female homozygous nude mice[15,19] (Taconic, Hudson, NY). Whole body BLI was performed using an MsFxPRO system (Carestream Molecular Imaging, CT, USA). Anesthetized animals were injected with D-Luciferin (Perkin-Elmer, MA, USA) and imaged 10 minutes post-administration to obtain a significant signal. All animal studies were approved by the Institutional Review Board for the Animal Care and Facilities Committee of Rutgers University and performed in accordance with institutional guidelines on animal handling.

Whole-animal SWIR imaging

A small animal SWIR imaging system was assembled in-house[15,19]. Mice were fully anesthetized using 2% isoflurane (Butler-Schein, Dublin, OH) and were continuously scanned with a collimated 980 nm laser (1.7 W). SWIR emission was detected with an InGaAs camera (Sensors Unlimited, Princeton, NJ) equipped with two 1,020 nm long-pass filters and a band-pass 1538/82 nm filter (Semrock, Rochester, NY) and a 25 mm focal length SWIR lens (StingRay Optics, Keene, NH). The system is capable of real-time animal imaging with an exposure time of 33 ms/frame. Images were acquired as video files and processed for quantitative analysis using custom Matlab scripts, as described in the section 'SWIR image analysis'. Animals injected with 200ul of ReANCs intravenously were imaged

at 20 fps and a representative video post-processed to show localization of particles is shown in Supplementary Video 1.

MRI and CT imaging

MR images are acquired using 1 Tesla M2 high-performance MRI system (Aspect Magnet Technologies Ltd, Netanya, Israel). CT images were acquired using ALBIRA PET/CT system (Carestream Molecular Imaging, CT, USA). All imaging procedures were performed under inhalation anesthesia with isoflurane at a concentration of 4% for induction of anesthesia and 1–2% for maintenance. Volumetric 3-D reconstruction to determine tumor volumes was performed using Vivoquant® software (Aspect Magnet Technologies, Israel). For contrast-enhanced MRI, pre-contrast Fast Spin Echo (FSE) and Gradient Echo (GRE) images were acquired followed by injection of Magnevist; Gadopentetic acid (Henry Schein, NY, USA) and acquisition of post-contrast GRE and FSE images. Analysis of T1 and T2 weighted images were performed as described under MRI image analysis.

Orthotopic model of bone metastasis

Bone-tropic MDA-MB-231 derived SCP2 cells expressing luciferase[18] (a gift from Dr. Kang, Princeton University) were maintained in Dulbecco's Modified Eagle Medium (DMEM) supplemented with 10% fetal bovine serum and 1% penicillin/streptomycin. 1×10^5 MDA-MB-231 derived SCP2 basal-like breast cancer cells were injected into the tibiae of 3–4 week old female homozygous athymic nude mice under inhalation anesthesia with 2–3% isothesia[7]. Whole body SWIR imaging was performed on all animals both pre- and post-ReANC injection (200 μL; 10 mg.kg^{-1}; i.v. administration via tail vein). Tumor progression was monitored longitudinally by using SWIR imaging weekly over a 10-week time course. SWIR intensity from the tibia of tumor-bearing and healthy control animals was quantified to determine the accumulation of ReANCs. The presence of tumor in the bone space was confirmed using BLI at week 9. MRI was used to monitor any bone deformities due to the presence of lytic lesions.

Biomimetic model of bone metastasis

Parental MDA_MB-231 and MDA-MB-231 derived SCP28 cells[18] (a kind gift from Dr. Kang, Princeton University) were maintained in DMEM supplemented with 10% fetal bovine serum and 1% penicillin/streptomycin. 3–4 week old homozygous female athymic nude mice were intravenously inoculated via the tail vein with the MDA-MB-231-derived SCP28 breast cancer cell line (2×10^5 cells; a gift from Dr. Kang, Princeton University; note that SCP28 are a subclonal population different from SCP2), leading to the development of lung and bone lesions[18]. Animals received weekly injections of ReANCs (200 μL, 10 mg/kg, via i.v. administration) to detect and monitor tumor progression over a 10-week time course. In another study, MDA-MB-231 cells (3×10^5 cells) were injected intravenously into 4–5 week old female athymic nude mice. Animals received weekly injections of ReANCs, fReANCs or a cocktail of ReANCs and fReANCs (200 μL, 10 mg/kg, via i.v. administration) to detect and monitor tumor progression over a 10-week time course. Whole body SWIR imaging was performed pre- and post- ReANC administration. Tumor burden was validated by bi-monthly MRI. CE-MRI was also performed to determine tumor burden in legs.

Biomimetic model of multi-organ distal metastases

Bone-derived MCF-7-5624A cells were maintained in DMEM supplemented with 10% fetal bovine serum and 1% penicillin/streptomycin[7]. The authenticity of the animal-derived line to the parental line was tested using the cell line authentication services using Short Tandem Repeat (STR) profiling (ATCC, VA). MCF-7-5624A tumor cells were injected into the left cardiac ventricle (5×10^5 cells) in 3–4 week old homozygous female athymic nude mice (Taconic, Hudson, NY) supplemented with low-dose estrogen pellets (0.18 mg; Innovative Research of America, Sarasota, FL) that deliver 2 μg/day of 17β estradiol. Tumor progression and size was monitored through BLI and MRI. Mice received weekly injections of ReANCs or fReANCs functionalized with 12.5 μM AMD3100 at 10 mg/kg body weight and were imaged immediately post injection and up to 24 hours post administration. SWIR signal from the leg bones and the dorsal area corresponding to the location of the adrenal glands was quantified. Animals were sacrificed upon weight loss and organs were excised. Tumor volume was calculated using 3D reconstructions generated from MRI imaging.

Ex vivo analysis of bone microlesions

At experimental endpoints, animals were euthanized and bones were excised and fixed in formalin. Bones were later decalcified in 0.5 M EDTA for 24–48 hours and stored at 4°C in 70% ethanol prior to processing. Tissues were then embedded in paraffin and 5 μm sections prepared. Tissue sections were de-paraffinized, rehydrated, and stained with H&E before mounting and imaging under standard light microscopy (Nikon, Chiyoda, Japan).

Ex vivo analysis of adrenal lesions

Adrenal tumors were removed, fixed in 10% neutral-buffered formalin overnight and stored at 4°C in 70% ethanol prior to processing. Tissues were then embedded in paraffin and 5 μm sections prepared. Tissue sections were de-paraffinized, rehydrated, and stained with hematoxylin and eosin (H&E), as well as with rabbit monoclonal anti-human ERα IgG (Catalog no: ab16660, Clone SP1, Spring Bioscience, CA) and rabbit monoclonal anti-human CXCR4 IgG antibody (Catalog no : ab181020, Clone EPUMBR3, Abcam, Cambridge,UK). Control slides were stained using appropriate isotype control antibodies. Biotinylated secondary antibodies were used for detection.

SWIR image analysis

SWIR emission from animals was collected pre-and post-injection of nanoparticles in the form of a video file in .bin format. A white light image of the animal for both time points was taken and labeled according to the condition. The bin file converting Matlab file was used to process the video files to extract maximum pixel values from each frame of the video and saved as a tiff image file. Image processing was done through manual selection of Regions Of Interest (ROI). ROIs corresponding to the desired organ were selected using anatomical landmarks present in background images. These ROIs were then applied to the associated infrared image, and the mean SWIR signal intensity over space for the region of interest was calculated. These values were then used to perform statistical analyses to compare the SWIR signal from each ROI between tumor-bearing and healthy control groups.

MRI image analysis

Post-contrast changes in signal intensity were quantified by exporting the images acquired using T2 MRI as dicom files and analyzing them using vivoquant software. Unique image scale factor for each image is extracted and applied to the individual image before quantification for normalization. Post normalization, the bone space of the animal is selected using the 3D ROI tool in vivoquant. The mean pixel intensity value in the selected 3D space is generated as an excel file by the software. The increase in pixel intensity due to contrast injection is evaluated by analyzing both pre and post contrast MRI scans. The increase of pixel intensity was compared between the tumor-bearing and healthy control animal groups.

Human soluble receptor array and human oncology array for molecular phenotyping

Organs bearing metastatic tumors were processed and the resulting cells collected and cultured. To isolate tumor cells from bone lesions, a 1 ml syringe with a 26G needle was filled with phosphate buffered saline (PBS) and inserted into one end of the tibia and cells expelled from the other end by applying positive pressure to the syringe. For adrenal and lung tumors, cells were crushed and homogenized using frosted glass slides and cells filtered to remove debris using a cell strainer (Falcon, USA). After one to two weeks of culture, a pure population of human cancer cells was obtained. Cell line protein expression was evaluated using with the Human Soluble Receptor Array Kit Non-Hematopoietic Panel or Human Oncology Array (R&D systems, Minneapolis, MN) according to the manufacturer's instructions. Array results were quantified in terms of pixel density using ImageJ (NIH, Bethesda MD) and the degree of fold-change was determined in comparison to that of the parental line.

Quantitative biodistribution, clearance and toxicology studies

Athymic nude mice were injected with 10mg/kg of ReANCs. Primary organs of clearance (liver, lung, kidney and spleen) were harvested at 0hr, 1 day, 3 days and 7 days post injection and imaged ex vivo using the SWIR imaging system. Ex vivo SWIR intensity was correlated to nanoparticle (yttrium) content in organs as determined by ICP-MS. Briefly, yttrium content of digested organs taken from mice was quantified using a Thermo X series II ICP-MS (Thermo Scientific, Waltham, MA) to determine particle concentration after injection. All samples were digested in 16 M nitric acid (Fisher Scientific, Waltham, MA) and evaporated to dryness, then reconstituted in 10% nitric acid to account for differences in sample volume. Count rates for yttrium were correlated to parts per billion using a standard curve generated with an yttrium standard (Sigma-Aldrich, Allentown, PA). Percentage of injected dose was calculated by correlating yttrium content in the injected nanoparticle dose to yttrium content per gram of tissue.

Competitive Inhibition of CXCR4 as a measure of passive targeting

MDA-MB-231 cells were cultured in DMEM (Gibco, Thermo Fisher Scientific) supplemented with 10% FBS and 1% penicillin-streptomycin. Cells were plated in a 96 well plate (Falcon, Corning Brand, Corning, NY) at a cell density of 100,000 cells per well. The ligand Stromal Cell-derived Factor-1α (SDF-1α) (PeproTech) was added to cells at concentrations of 10 nM, and 100 nM and incubated in 37°C for 2 hours. Following this,

cells were treated with ReANC and fReANCs and incubated at 37°C for 15–18 hours. Cells were fixed in 1% paraformaldehyde subsequent to trypsinization and washes. The samples were then analyzed via Fluorescence Assisted Cell Sorting (FACS) (FACs caliber, BD biosciences, CA) and uptake quantified as a function of green fluorescence from the albumin shell. Data were analyzed using Kaluza Analysis software (Beckman Coulter, CA).

In vitro optimization of nanoprobes

Scratch and cell migration assays were used to determine the effect of AMD 3100 functionalization on cell mobility. In the scratch assay, MCF7 cells were plated in 6 well plates and allowed to grow until confluent. These cell monolayers were scored with a pipette tip and samples were treated with varying concentrations of ReANCs, fReANCs, and free AMD3100 in solution. The scratches were imaged over the course of 24 hours to measure wound closure and cellular movement into the scratch. Cell migration was evaluated by measuring cell movement through 8 uM transwell inserts. MDA-MB-231 cells were plated on top of 8 uM transwell inserts and treated with ReANCs, fReANCs, and free AMD3100 in solution. Cells were then allowed to migrate through the mesh. Cell migration was evaluated through microscopy and crystal violet staining.

Statistical analysis

For all in vivo studies, animal number was determined using G-power analysis (ANOVA, one-way, omnibus) providing at least 70–80% power and an effect size of 0.8–0.85, with α set at 0.05. Full experimental details are provided in the methods section(s) above, to ensure independent reproducibility by other investigators. For all in-vivo studies, mice were randomly assigned to each experimental or control group and investigators were not blinded to the groups through the process of acquiring and analysis of data. Grubb's test for outliers was used to determine the inclusion or exclusion of data within groups for all data sets. The similarity of the variance between the groups was tested using the F-test of equality of variances using a confidence interval of 95%. Statistical tests were selected based on the normality of the distribution, sample size and the similarity in variance between groups. Statistical significance of the normal populations and was determined using a two-tailed student t- test or Welch's t-test. All statistical analysis was done using graphpad prism version 7.0.

Code availability

Three MATLAB image-processing scripts are available on Github (https://github.com/markpierce50/Nature-BME-2017/releases/latest).

Data availability

The data that support the findings of this study are available within the paper and its supplementary information.

Supplementary Material

Refer to Web version on PubMed Central for supplementary material.

Acknowledgments

References

1. Kennecke H, et al. Metastatic behavior of breast cancer subtypes. Journal of clinical oncology : official journal of the American Society of Clinical Oncology. 2010; 28:3271–3277. DOI: 10.1200/JCO.2009.25.9820 [PubMed: 20498394]

2. Chaffer CL, Weinberg RA. A perspective on cancer cell metastasis. Science. 2011; 331:1559–1564. DOI: 10.1126/science.1203543 [PubMed: 21436443]

3. Dawood S, Broglio K, Ensor J, Hortobagyi GN, Giordano SH. Survival differences among women with de novo stage IV and relapsed breast cancer. Annals of oncology : official journal of the European Society for Medical Oncology / ESMO. 2010; 21:2169–2174. DOI: 10.1093/annonc/mdq220

4. Dawood S, et al. Differences in survival among women with stage III inflammatory and noninflammatory locally advanced breast cancer appear early: a large population-based study. Cancer. 2011; 117:1819–1826. DOI: 10.1002/cncr.25682 [PubMed: 21509759]

5. Manders K, et al. Clinical management of women with metastatic breast cancer: a descriptive study according to age group. BMC cancer. 2006; 6:179. [PubMed: 16824210]

6. Plunkett TA, Smith P, Rubens RD. Risk of complications from bone metastases in breast cancer. implications for management. European journal of cancer. 2000; 36:476–482. [PubMed: 10717523]

7. Ganapathy V, et al. Luminal breast cancer metastasis is dependent on estrogen signaling. Clinical & experimental metastasis. 2012; 29:493–509. DOI: 10.1007/s10585-012-9466-4 [PubMed: 22427027]

8. Ganapathy V, et al. Targeting the Transforming Growth Factor-beta pathway inhibits human basal-like breast cancer metastasis. Molecular cancer. 2010; 9:122. [PubMed: 20504320]

9. Setyawati MI, Tay CY, Docter D, Stauber RH, Leong DT. Understanding and exploiting nanoparticles' intimacy with the blood vessel and blood. Chem Soc Rev. 2015; 44:8174–8199. DOI: 10.1039/c5cs00499c [PubMed: 26239875]

10. Cleaver O, Melton DA. Endothelial signaling during development. Nat Med. 2003; 9:661–668. DOI: 10.1038/nm0603-661 [PubMed: 12778164]

11. Barua S, Mitragotri S. Challenges associated with Penetration of Nanoparticles across Cell and Tissue Barriers: A Review of Current Status and Future Prospects. Nano Today. 2014; 9:223–243. DOI: 10.1016/j.nantod.2014.04.008 [PubMed: 25132862]

12. Blanco E, Shen H, Ferrari M. Principles of nanoparticle design for overcoming biological barriers to drug delivery. Nat Biotechnol. 2015; 33:941–951. DOI: 10.1038/nbt.3330 [PubMed: 26348965]

13. Smith AM, Mancini MC, Nie S. Bioimaging: second window for in vivo imaging. Nat Nanotechnol. 2009; 4:710–711. nnano.2009.326[pii]. DOI: 10.1038/nnano.2009.326 [PubMed: 19898521]

14. Sordillo LA, Pu Y, Pratavieira S, Budansky Y, Alfano RR. Deep optical imaging of tissue using the second and third near-infrared spectral windows. Journal of biomedical optics. 2014; 19:056004. [PubMed: 24805808]

15. Naczynski DJ, et al. Rare-earth-doped biological composites as in vivo shortwave infrared reporters. Nature communications. 2013; 4:2199.

16. van Saders B, Al-Baroudi L, Tan MC, Riman RE. Rare-earth doped particles with tunable infrared emissions for biomedical imaging. Opt Mater Express. 2013; 3:566–573. DOI: 10.1364/OME.3.000566

17. Tan MC, Connolly J, Riman RE. Optical Efficiency of Short Wave Infrared Emitting Phosphors. The Journal of Physical Chemistry C. 2011; 115:17952–17957. DOI: 10.1021/jp203735n

18. Kang Y, et al. A multigenic program mediating breast cancer metastasis to bone. Cancer cell. 2003; 3:537–549. [PubMed: 12842083]

19. Zevon M, et al. CXCR-4 Targeted, Short Wave Infrared (SWIR) Emitting Nanoprobes for Enhanced Deep Tissue Imaging and Micrometastatic Cancer Lesion Detection. Small. 2015; 11:6347–6357. DOI: 10.1002/smll.201502202 [PubMed: 26514367]

20. Zhao X, He S, Tan MC. Design of infrared-emitting rare earth doped nanoparticles and nanostructured composites. Journal of Materials Chemistry C. 2016; 4:8349–8372. DOI: 10.1039/C6TC02373H

21. Sheng Y, De Liao L, Thakor NV, Tan MC. Nanoparticles for Molecular Imaging. Journal of Biomedical Nanotechnology. 2014; 10:2641–2676. DOI: 10.1166/jbn.2014.1937 [PubMed: 25992413]

22. Naczynski DJ, et al. Albumin Nanoshell Encapsulation of Near-Infrared-Excitable Rare-Earth Nanoparticles Enhances Biocompatibility and Enables Targeted Cell Imaging. Small. 2010; 6:1631–1640. DOI: 10.1002/smll.200902403 [PubMed: 20586056]

23. Hendrix CW, et al. Pharmacokinetics and safety of AMD-3100, a novel antagonist of the CXCR-4 chemokine receptor, in human volunteers. Antimicrob Agents Chemother. 2000; 44:1667–1673. [PubMed: 10817726]

24. De Clercq E. The bicyclam AMD3100 story. Nat Rev Drug Discov. 2003; 2:581–587. DOI: 10.1038/nrd1134 [PubMed: 12815382]

25. Baglioni M, et al. Binding of the doxorubicin-lactosaminated human albumin conjugate to HCC cells is mediated by the drug moieties. Dig Liver Dis. 2008; 40:963–964. DOI: 10.1016/j.dld.2008.05.014 [PubMed: 18606580]

26. Kratz F. Albumin as a drug carrier: design of prodrugs, drug conjugates and nanoparticles. J Control Release. 2008; 132:171–183. DOI: 10.1016/j.jconrel.2008.05.010 [PubMed: 18582981]

27. Ulmert D, Solnes L, Thorek D. Contemporary approaches for imaging skeletal metastasis. Bone Res. 2015; 3:15024. [PubMed: 26273541]

28. Minn AJ, et al. Genes that mediate breast cancer metastasis to lung. Nature. 2005; 436:518–524. DOI: 10.1038/nature03799 [PubMed: 16049480]

29. Minn AJ, et al. Distinct organ-specific metastatic potential of individual breast cancer cells and primary tumors. The Journal of clinical investigation. 2005; 115:44–55. DOI: 10.1172/JCI22320 [PubMed: 15630443]

30. Toy R, Peiris PM, Ghaghada KB, Karathanasis E. Shaping cancer nanomedicine: the effect of particle shape on the in vivo journey of nanoparticles. Nanomedicine (Lond). 2014; 9:121–134. DOI: 10.2217/nnm.13.191 [PubMed: 24354814]

31. Berman AT, Thukral AD, Hwang WT, Solin LJ, Vapiwala N. Incidence and patterns of distant metastases for patients with early-stage breast cancer after breast conservation treatment. Clin Breast Cancer. 2013; 13:88–94. DOI: 10.1016/j.clbc.2012.11.001 [PubMed: 23218473]

32. Sethi N, Kang Y. Notch signalling in cancer progression and bone metastasis. British journal of cancer. 2011; 105:1805–1810. DOI: 10.1038/bjc.2011.497 [PubMed: 22075946]

33. Hazan RB, Phillips GR, Qiao RF, Norton L, Aaronson SA. Exogenous expression of N-cadherin in breast cancer cells induces cell migration, invasion, and metastasis (vol 148, pg 779, 2000). J Cell Biol. 2000; 149:239–239.

34. Gligorijevic B, et al. Intravital Imaging and Photoswitching in Tumor Invasion and Intravasation Microenvironments. Micros Today. 2010; 18:34–37. DOI: 10.1017/S1551929510991220 [PubMed: 25635177]

35. Hulit J, et al. The use of fluorescent proteins for intravital imaging of cancer cell invasion. Methods in molecular biology. 2012; 872:15–30. DOI: 10.1007/978-1-61779-797-2_2 [PubMed: 22700401]

36. Kedrin D, et al. Intravital imaging of metastatic behavior through a mammary imaging window. Nat Methods. 2008; 5:1019–1021. DOI: 10.1038/nmeth.1269 [PubMed: 18997781]

37. Fein MR, Egeblad M. Caught in the act: revealing the metastatic process by live imaging. Dis Model Mech. 2013; 6:580–593. DOI: 10.1242/dmm.009282 [PubMed: 23616077]

38. Lunov O, et al. Differential uptake of functionalized polystyrene nanoparticles by human macrophages and a monocytic cell line. ACS nano. 2011; 5:1657–1669. DOI: 10.1021/nn2000756 [PubMed: 21344890]

39. Suva LJ, Griffin RJ, Makhoul I. Mechanisms of bone metastases of breast cancer. Endocr Relat Cancer. 2009; 16:703–713. DOI: 10.1677/ERC-09-0012 [PubMed: 19443538]

40. Murugan K, et al. Parameters and characteristics governing cellular internalization and trans-barrier trafficking of nanostructures. Int J Nanomedicine. 2015; 10:2191–2206. DOI: 10.2147/ IJN.S75615 [PubMed: 25834433]

41. Bertrand N, Wu J, Xu X, Kamaly N, Farokhzad OC. Cancer nanotechnology: the impact of passive and active targeting in the era of modern cancer biology. Adv Drug Deliv Rev. 2014; 66:2–25. DOI: 10.1016/j.addr.2013.11.009 [PubMed: 24270007]

42. Kettiger H, Schipanski A, Wick P, Huwyler J. Engineered nanomaterial uptake and tissue distribution: from cell to organism. Int J Nanomedicine. 2013; 8:3255–3269. DOI: 10.2147/ IJN.S49770 [PubMed: 24023514]

43. Kang Y, Pantel K. Tumor cell dissemination: emerging biological insights from animal models and cancer patients. Cancer cell. 2013; 23:573–581. DOI: 10.1016/j.ccr.2013.04.017 [PubMed: 23680145]
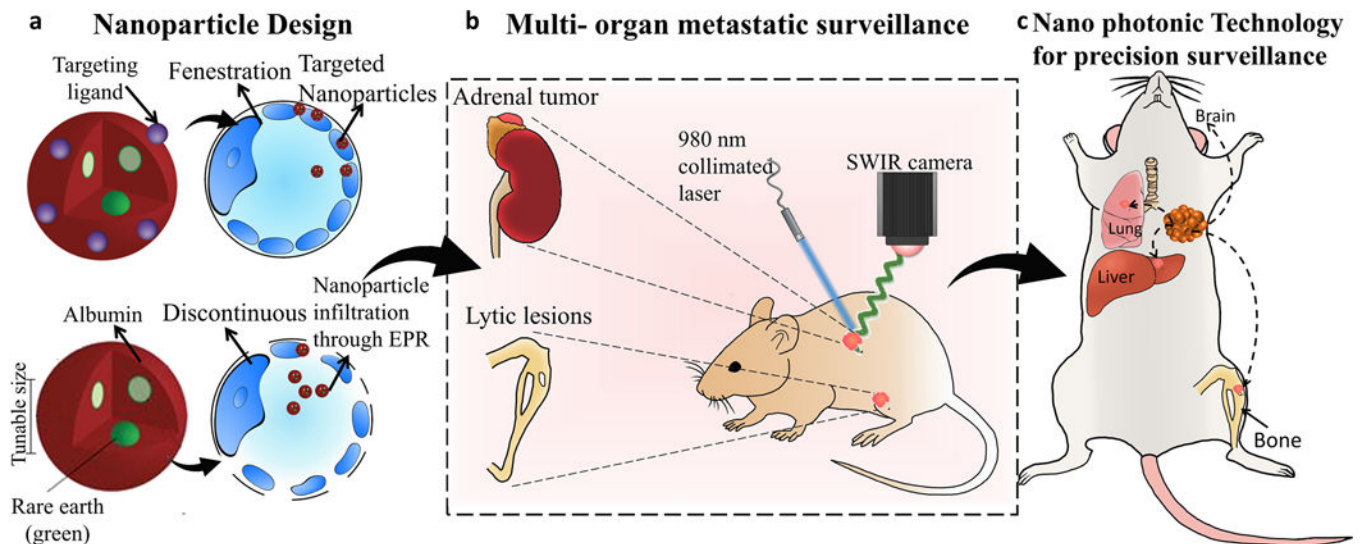
Figure 1. Design and workflow of photonic nanotechnology for cancer-metastasis detection and profiling

Distinct nanoparticles were designed with rare-earth-doped cores based on differences in tissue microenvironment (a) to enable whole body screening based on deeper-tissue emanating short-wave infrared emissions. When administered *in vivo* to biomimetic breast cancer models, these nanoparticles are targeted to reach multi-organ metastatic sites across different pharmacologic barriers(b). Metastatic lesions (in the long bones or adrenal glands) can be detected earlier than conventional methods (bioluminescence, MRI, CT) and molecular changes in cancer cell signatures can be obtained, forming the basis for future metastatic-site specific, personalized cancer therapies(c).
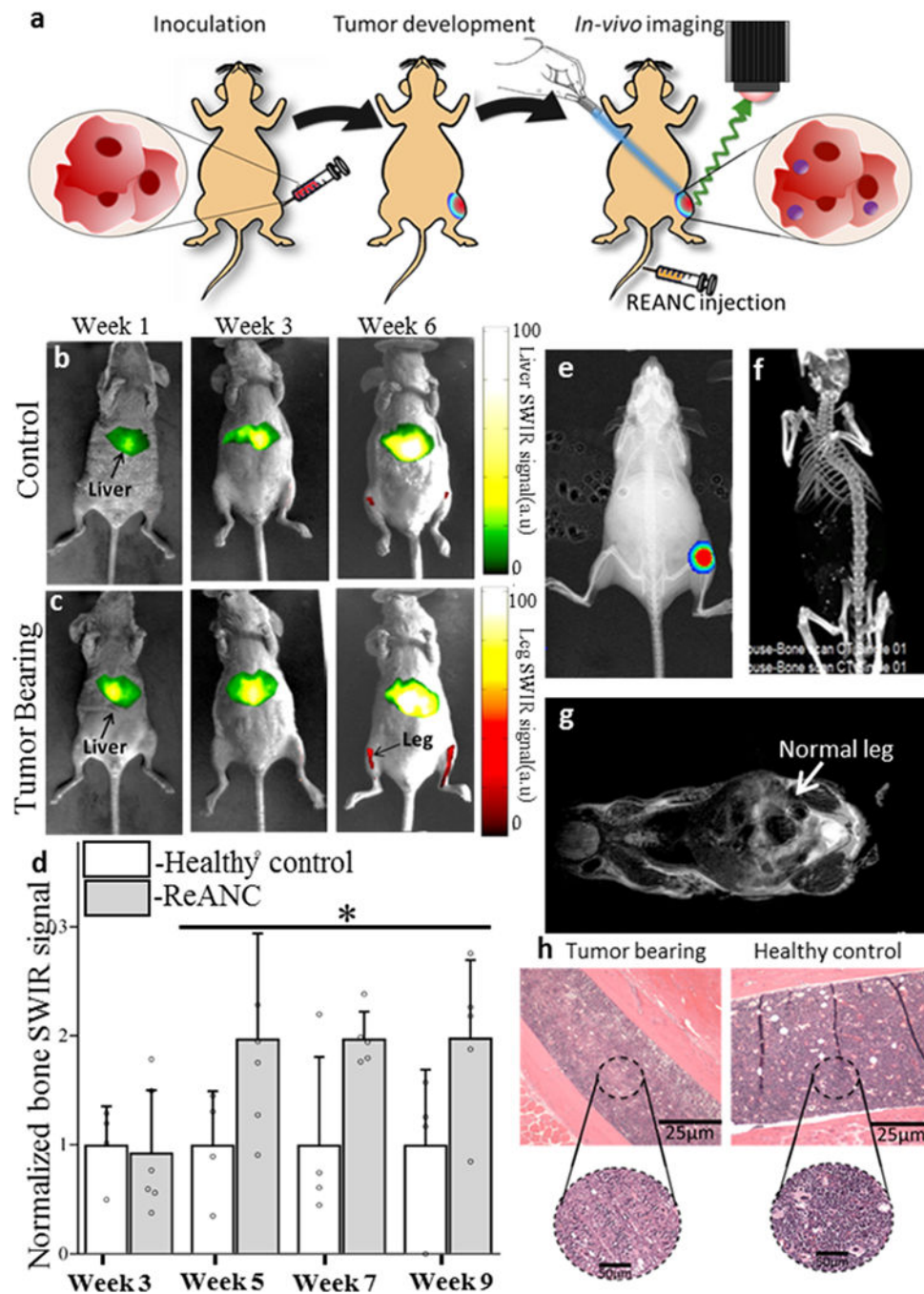
Figure 2. SWIR imaging of photonic nanoparticles discerns bone lesions *in vivo* that are undetectable by conventional MRI and CT

(a) Schematic diagram illustrating intra-tibial inoculation of MDA-MB-231 derived SCP2 cells followed by tail vein administration of ReANCs and *in vivo* SWIR imaging. Representative SWIR images from (b) healthy (non-tumor-bearing) animals and (c) tumor-bearing mice. (d) Quantification of SWIR signal in the tibiae of tumor-bearing and healthy controls shows a 2-fold increase in signal at 5-weeks post inoculation. Data is expressed as mean±S.D; n=6 for tumor-bearing group and n=3 for healthy control group. *P<0.1, determined by Welch's t-test. Data in (d) is represented as a fold increase compared to

healthy control. (e) Validation of tumor presence by BLI. (f) End point CT and (g) MRI do not indicate bone deformities while (h) *ex vivo* histopathology shows possible hypo-cellularization, potentially indicating lytic activity due to the presence of tumors in tumor-bearing legs compared to healthy controls. SWIR intensities were normalized to those of the healthy control groups for the region of interest at each time point.
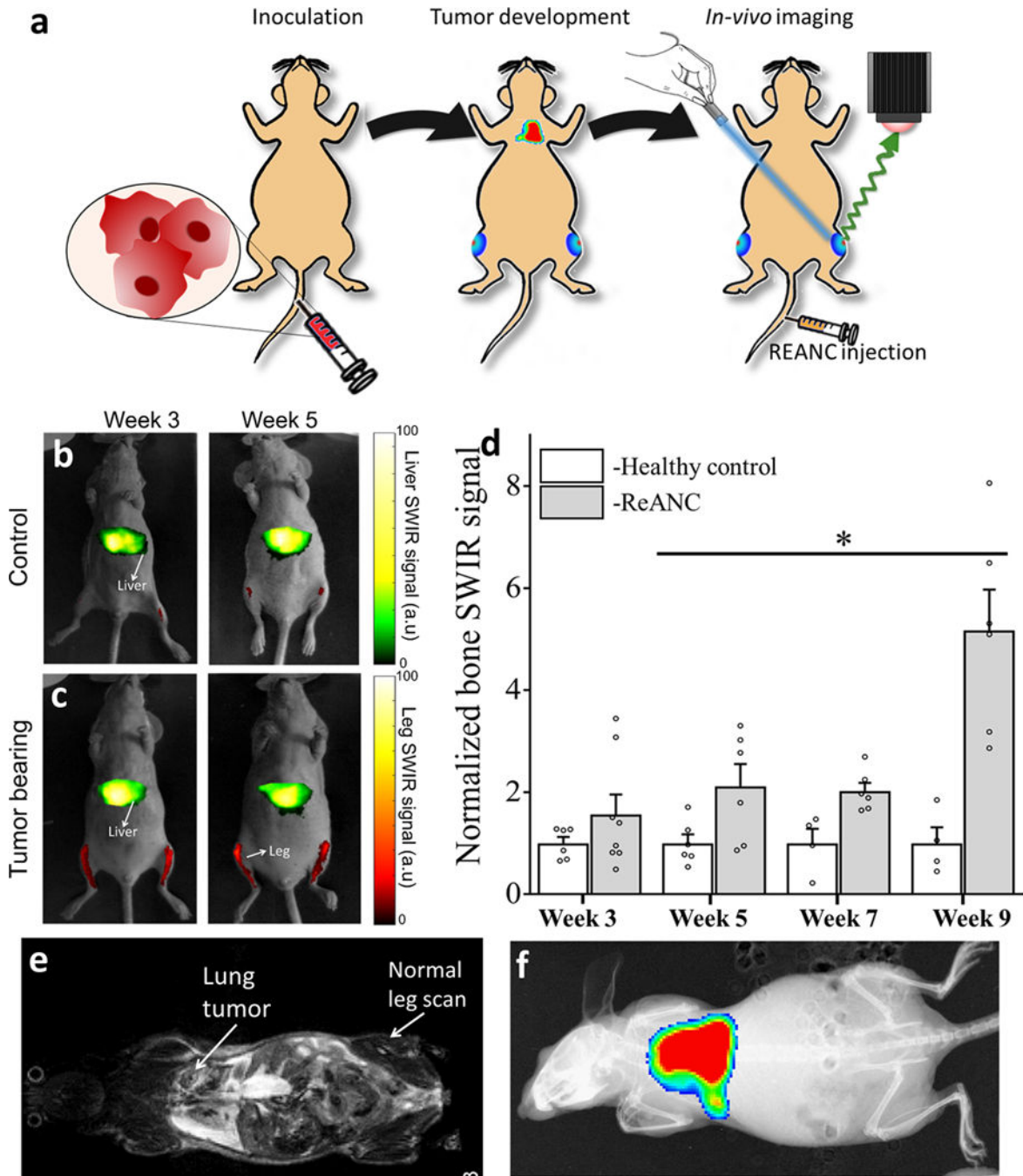
Figure 3. Distal bone lesions can be detected with SWIR imaging earlier than by MRI and CT in a biomimetic metastasis model

(a) Schematic diagram illustrating intravenous inoculation of MDA-MB-231 derived SCP28 cells followed by tail vein administration of ReANCs and *in vivo* SWIR imaging. Representative images from (b) non-tumor-bearing control animals and (c) tumor-bearing animals at weeks 3 and 5 post-inoculation. (d) Quantification of SWIR intensity shows at least a 2-fold increase in signal over healthy controls from week 5 onwards. Data is expressed as mean±S.D; n=4 for tumor-bearing group and n=3 for healthy control group. *two-tailed P<0.06, determined by Welch's t-test. Data in (d) is represented as a fold

increase compared to healthy control. (e) MRI and (f) BLI show no visible bone abnormalities at the study end point. SWIR intensities were normalized to those of the healthy control groups for the region of interest at each time point.
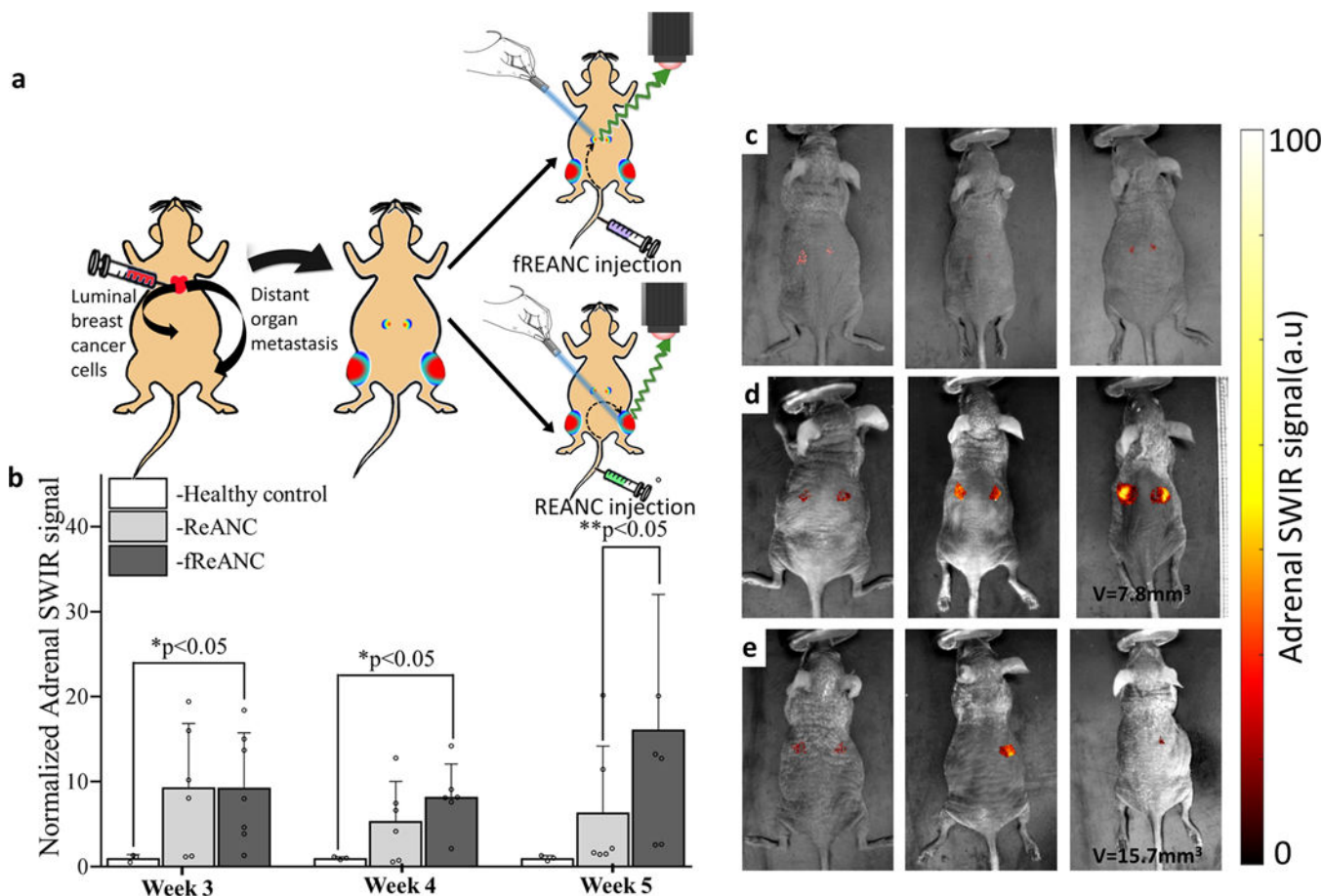
Figure 4. Differential niche-based accumulation of ReANC and fReANC formulations leads to multi-organ detection of metastases in a luminal breast cancer model

(a) Athymic nude mice were injected with MCF7 derived cells via the left ventricle to form[15] metastases in adrenals and bones; (b) Weekly intravenous administration of fReANCs show earlier detection of adrenal metastases compared to untargeted ReANCs. Quantitative analysis of SWIR intensity shows significantly higher accumulation of fREANCs compared to ReANCs at 5 weeks post inoculation whereas comparison between healthy controls and tumor-bearing animals injected with fReANC shows higher SWIR signal from adrenal lesions as early as 3 weeks post inoculation. Volumetric MRI analysis found the smallest tumor volume detected 5-weeks post inoculation with fReANCs to be 7.8 mm^3, compared to a volume of 15.7 mm^3 with REANCs. Representative dorsal (prone) images showing SWIR signal from adrenal lesions of healthy controls (c) and tumor-bearing animals injected with fReANC (d) and ReANC(e) shows earlier detection of adrenal metastases with active targeting. Data in (b) is expressed as mean±S.D; n=6 for tumor-bearing group and n=3 for healthy control group. *two-tailed P<0.05, determined by Welch's t-test. ** two-tailed P<0.05, determined by Welch's t-test. SWIR intensities were normalized to those of the healthy control groups for the region of interest at each time point.
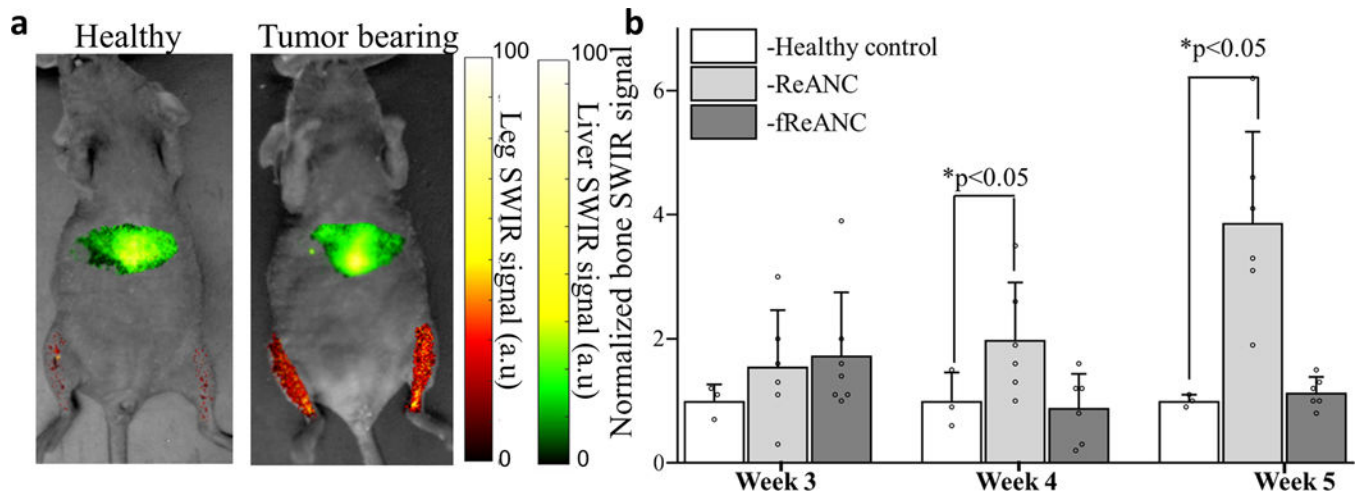
Figure 5. Passive accumulation of ReANCs, via the discontinuous fenestration architecture of bone tissue, in a metastatic luminal breast cancer model

Athymic nude mice were injected with MCF7 derived cells via the left ventricle to form metastases in bones followed by weekly injections of ReANC nanoprobes. (a) Representative ventral (supine) images showing SWIR signal from the bone space of tumor-bearing and healthy control animals show significant accumulation of ReANCs in the bone lesions 5 weeks post inoculation. (b) There is significant increase in SWIR emission intensity in bone starting 4 weeks post inoculation in tumor-bearing and healthy controls injected with ReANCs. There was no significant increase in accumulation of fReANC in bones of tumor-bearing and healthy control animals. Data in (b) is expressed as mean±S.D; n=6 for tumor-bearing group and n=3 for healthy control group represented as a fold increase compared to healthy control group.*two-tailed P<0.05 determined using a Welch's t-test. SWIR intensities were normalized to those of the healthy control groups for the region of interest at each time point.
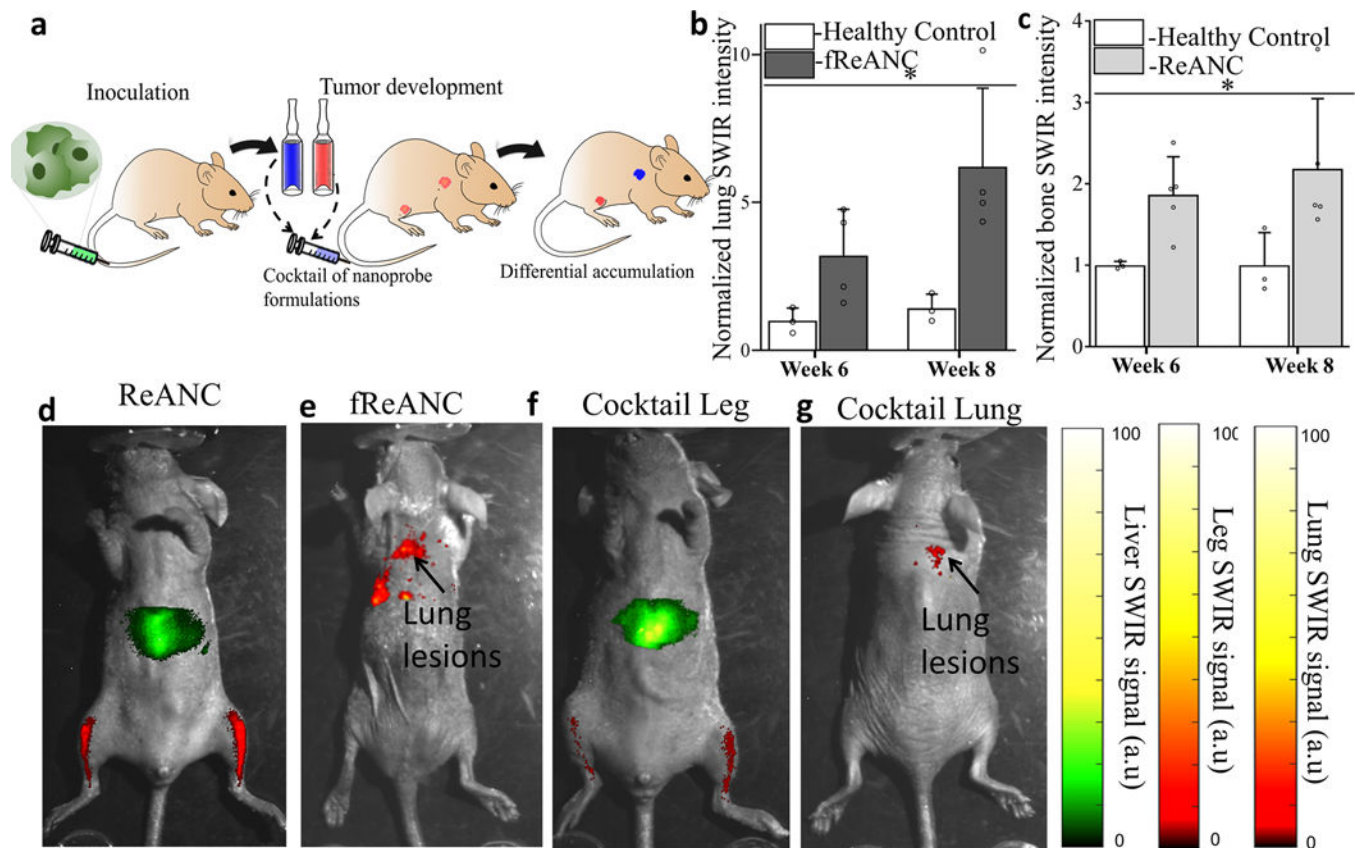
Figure 6. Differential accumulation of ReANCs in leg lesions and fReANCs in lung lesions in a multi-organ metastatic model

(a) Schematic illustrating intravenous inoculation of MDA-MB-231 cells followed by intravenous administration of a cocktail of nanoprobe formulations and SWIR imaging. Quantitative analysis of SWIR signal shows significantly higher lung intensity compared to healthy controls (b). Representative images show localization of ReANC localization to leg lesions (c); and fReANC localization to lung lesions (d). Representative animal injected with a cocktail of ReANC and fReANC probes showed leg signal (e) and lung signal (f). Data is expressed as mean ± S.D; n=4 for tumor-bearing group and n=3 for healthy control group represented as fold increase compared to healthy control group. *p<0.07, determined by Welch's t test. SWIR intensities were normalized to those of the healthy control groups for the region of interest at each time point.
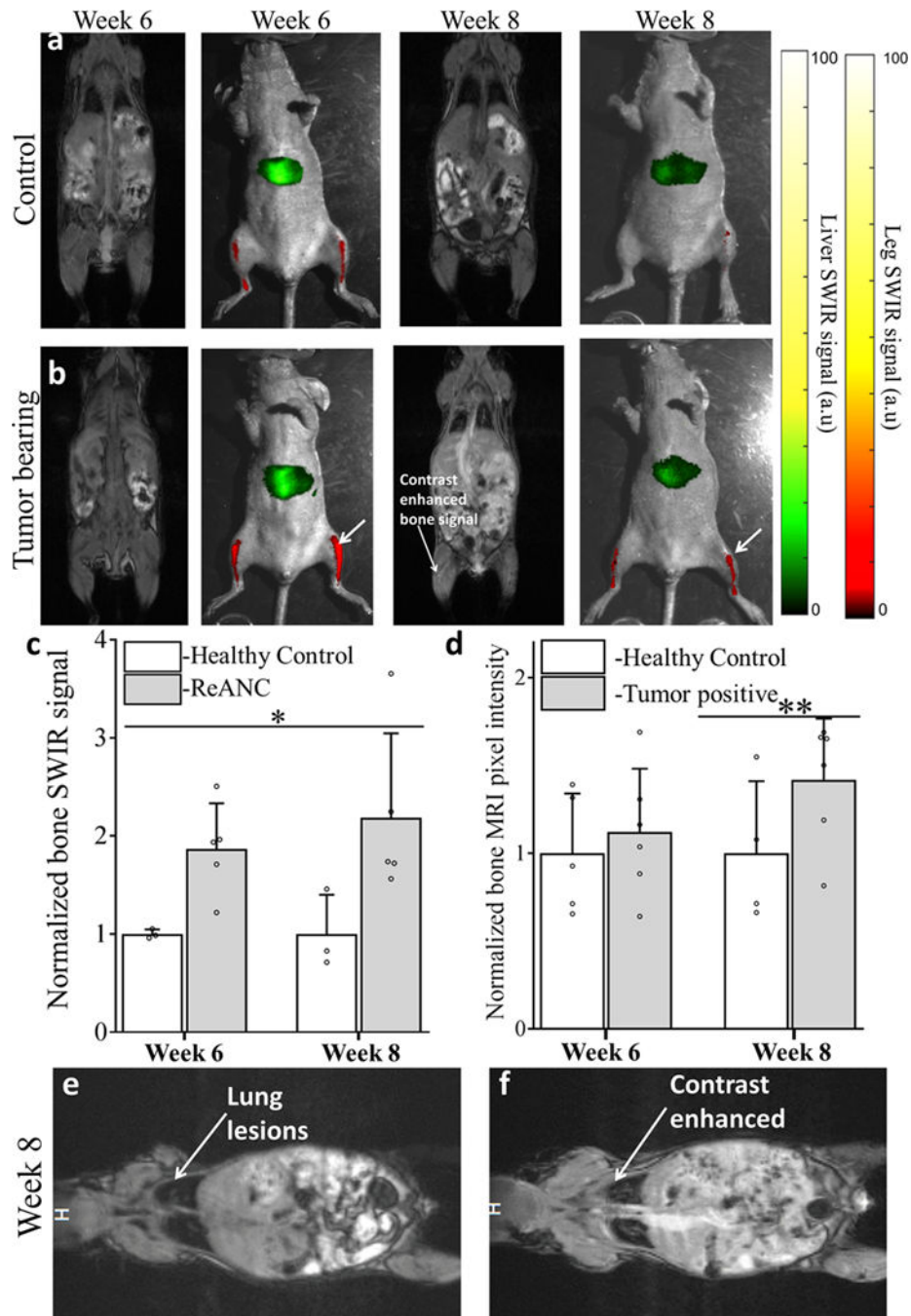
Figure 7. Distal bone lesions can be detected with SWIR imaging earlier than by contrast-enhanced MRI in a biomimetic metastasis model

Representative images from non-tumor control animals (a) and Tumor-bearing animals (b) shows enhanced SWIR signal 6 weeks' post inoculation with no significant changes in CE-MRI. At 8 weeks' post inoculation both SWIR and CE-MRI shows enhanced signal from the bone space. Quantitative comparison of SWIR emission intensity (c) in bone lesions shows significant increase starting week 6 post inoculation compared to non-tumor control animals. Quantitative analysis of increase in pixel intensity pre- and post-contrast injection in MR imaging does not show significant enhancement until week 8 (d). Representative image of

lung metastases prior to (e) and post (f) contrast injection at week 8, used as positive control, to show enhanced uptake of MRI contrast by tumor lesions. Data is expressed as mean± S.D; n=5 for tumor-bearing group and n=3 for healthy control group. *two-tailed P<0.05, determined by Welch's t-test; n=5 **two tailed P<0.05 determined by Welch's t-test; n=6. Data in c and d is represented as a fold increase compared to healthy control. SWIR intensities were normalized to those of the healthy control groups for the region of interest at each time point.

Table 1

Distinct metastatic lesions originating from a common cell line exhibit niche-dependent molecular signatures

Cancerous cells isolated from adrenal and bones were cultured ex vivo and analyzed for changes in biomarker expression with a hematopoietic array. Cellular markers upregulated in adrenal-tropic lines were typically associated with increased tumor growth and invasion, while those upregulated in the bone-tropic line act to promote bone resorption

PROTEINS UPREGULATED IN ADRENAL-TROPIC MCF7-6124A CELLS			
Protein	**Fold Change**	**Pathway activated**	**Clinical relevance**
N-Cadherin	4.75	Sustains activation of ERK and activates MMP-9 production	Promotes invasive activity and increases tumor metastasis
ADAM17	6.5	Activates EGFR-MEK-ERK pathway and upregulates MMP-2 and MMP-9, stimulates the release of TGFα	Increases cellular invasion and proliferation
JAM-A	4.5	Activates Rap1 GTPase and upregulates β1-integrin	Increases cell motility Indicates poor patient prognosis
PROTEINS UPREGULATED IN BONE-TROPIC MCF7-5624A CELLS			
Notch-1	2	Activated by downstream products of TGFβ-SMAD pathway to promote osteoclast differentiation in bone	Promotes bone reabsorption and osteolytic lesions
Amphiregulin	2	Stimulates and increases EGFR signaling	Important for bone colonization
EGFR	2.27	Activation with MMP-1 leads to reduced production of osteoprotegrin, increasing RANKL activation of osteoclasts	Impacts recruitment of osteoblasts, limiting bone mineralization